atmosphere

*Article*

# Meteorological Modulation of Atmospheric Boundary Layer Height over a Caribbean Island

**Alejandro Álvarez-Valencia [1], Juan L. Colón-Perez [1], Mark R. Jury [1,2,*] and Héctor J. Jiménez [1]**

[1] Physics Department, University of Puerto Rico, Mayaguez, PR 00681, USA
[2] Geography Department, University of Zululand, KwaDlangezwa 3886, South Africa
* Correspondence: mark.jury@upr.edu

**Abstract:** This study analyzes fluctuations in the atmospheric boundary layer height (aBLH) over a Caribbean island using hourly measured and model-interpolated data from the 2019–2023 period. Our focus is the mean structure, diurnal cycle, and aBLH correlation with meteorological parameters on the leeward coast at Mayaguez (18.2 N, 67.1 W). The mean diurnal cycle of the aBLH increases from 300 m near sunrise (07:00) to 1200 m by 13:00 because of turbulent heating. Summer-time thermal circulations lead to a 3 °C increase in near-surface dewpoint temperature (Td) that propagates upward to 3000 m by 16:00. A case study demonstrates how mid-day trade winds turn onshore and generate significant rainfall and river discharge across the island. The context for this study is provided by a 24 yr cluster analysis that identifies rainfall over the island's northwest interior driven by upstream heating. Analysis of linear trends from 1979 to 2023 shows that Td declined by −0.02 °C/yr above 1500 m because of large-scale subsidence. However, cool interior forests transpire humidity and instill contrasting trends that may amplify climate extremes. A better understanding of entrainment at the top of the atmospheric boundary layer could be critical for managing future water resources in Caribbean islands.

**Keywords:** atmospheric boundary layer height; diurnal cycle; island wake

**Citation:** Álvarez-Valencia, A.; Colón-Perez, J.L.; Jury, M.R.; Jiménez, H.J. Meteorological Modulation of Atmospheric Boundary Layer Height over a Caribbean Island. *Atmosphere* **2024**, *15*, 1007. https://doi.org/10.3390/atmos15081007

Academic Editor: Yubin Li

Received: 29 June 2024
Revised: 15 August 2024
Accepted: 18 August 2024
Published: 20 August 2024

## 1. Introduction

The sub-tropical climate is diurnally modulated by net solar radiation > 700 W/m$^2$ capped by subsidence from marine anticyclones and the Hadley circulation. Marine rainfall tends to crest before sunrise, while terrestrial rainfall peaks before sunset [1–3]. In the presence of a large island like Puerto Rico, frictional slowing of trade winds and helical land–sea breeze circulations alter the airflow and its buoyancy, promoting westward cloud bands [4–6]. Cascading processes have been revealed by analysis of surface turbulence, subtropical winds, atmospheric boundary layer height (aBLH), and convective life cycle. Diurnal heating precedes the moisture response, except under disturbed weather when morning cloud cover inhibits amplitude. The authors of [7] note that aBLH growth over flat terrain is associated with local turbulence, whereas advection by thermally driven airflow becomes important over mountainous terrain.

During quiescent weather and clear skies, the aBLH adjusts in sequence as follows: (i) stably stratified nocturnal conditions, (ii) sharp growth after sunrise, (iii) turbulent mid-day convection, and (iv) uneven collapse near sunset. Metrics for the aBLH involve the depth of surface turbulence estimated by an inflection point in vertical profiles of aerosol concentrations [8], temperature–humidity indices, and wind velocity. Even the tallest towers cannot reach the convective aBLH, while weather balloons are too infrequent. The authors of [9] employed a variety of methods to determine the aBLH. Proxies like the Richardson number yielded shallow estimates, while indices such as equivalent potential temperature produced deep values. Wind profiles from radar and commercial aircraft can identify the aBLH via Ekman turning of surface airflow toward lower pressure [10].

Technological advances in satellite and in situ passive infrared (IR) and microwave (MW) profilers and active radars offer new ways to quantify the aBLH [11,12], but these are prone to rain ambiguities that can be minimized via model diagnostics [13]. It appears that every method to ascertain how the atmospheric boundary layer responds to heat, moisture, and momentum fluxes is conditional.

Here, we aim to answer the following scientific questions: (i) how does the aBLH and Td profile vary over Puerto Rico, (ii) what modulates the aBLH over diurnal, seasonal, and inter-annual timescales, (iii) what distinguishes the role of local heat fluxes and mesoscale circulations, and (iv) is meteorological modulation of the aBLH under-represented in models? Data and methods that bring out the diurnal cycle are described in Section 2. Section 3 provides statistical results of measured and modeled the aBLH over Puerto Rico and examples of modulation across various time scales, without explicitly validating performance. Conclusions are given in Section 4.

## 2. Data and Methods

Air and dewpoint temperature, the aBLH, surface latent and sensible heat fluxes, net solar radiation, zonal and meridional wind (U V), vertical motion (W), and rainfall were evaluated from GPM, CFS2, and ERA5 products [14–16]. The spatial structure was analyzed within the following area: 17.2–19.1 N, 68.1–64.9 W. Hourly time series on the leeward coast at Mayaguez (18.21 N, 67.14 W) in the period 2019–2023 were extracted for analysis, using methods consistent with [17].

UPRM operates a passive MW profiler at Mayaguez (18.21° N, 67.14° W) to measure temperature–humidity indices from received signals at 5–6 mm and 10–15 mm [18,19]. The MW absorption lines broaden near the surface to enable vertical profiles from 50 m to 10 km. Mean hourly profiles and mean diurnal cycles were calculated for dewpoint temperature (Td) each season over the period March 2023–February 2024. Td was chosen because it is conserved over the diurnal cycle and only changes in response to kinematic and thermodynamic processes. Dewpoint temperature is routinely evaluated in radiosonde profiles and weather forecasts.

Hourly CFS2 and ERA5 reanalysis data were evaluated for the mean diurnal cycle at Mayagüez in the period 2019–2023 (N = 43,830). Box–whisker statistics were calculated to identify the mean, median, variance, amplitude, and phase over the 24 h cycle. Lag correlations were analyzed between the hourly aBLH and latent and sensible heat flux, net solar radiation, U wind, and rain, where 95% confidence was reached by $r > |0.4|$. Hourly data from the NOAA Mayagüez harbor weather station (18.22 N, 67.16 W) were evaluated by calculating the wind frequency distribution and the mean diurnal cycle of zonal wind and air temperature in 2023. Successive profiles of daily NCEP2 reanalysis Td were evaluated for synoptic weather pulsing in 2019–2023; this dataset incorporates radiosonde, aircraft, and satellite measurements (cf. https://space.oscar.wmo.int/gapanalyses?variable=80, accessed on 1 January 2024).

To place the results in context, an empirical orthogonal function (EOF) cluster analysis of GPM monthly rainfall from 2000 to 2023 was calculated [20], using WMO-KNMI Climate Explorer subroutines, to identify the leading modes around Puerto Rico (17.2–19.1 N, 68.1–64.9 W). Principal component time scores for modes one and two were extracted (PC1, PC2), representing marine and terrestrial clusters, respectively. The mean annual cycle was evaluated, and PC2 time scores were correlated with a variety of meteorological fields to understand the inter-annual modulation of summer rainfall over Puerto Rico. Hannachi et al. (2007) provide a comprehensive review of EOF analysis and its application to meteorological field data [20].

Background linear trends were computed within NCEP2 wind fields from 1979 to 2023 [21] and in MODIS IR satellite land surface temperature from 2000 to 2023 [22] using IRI Climate Library subroutines. Linear trends in Td, U, V, and W wind profiles from 1979 to 2023 were evaluated in the layer 1000–600 hPa (0–4000 m). A case study that describes the impact of diurnal sea breezes on 9 July 2023 was analyzed using Hysplit back-trajectories [23], 5 km resolution Chirp rainfall [24], and NAM wind profiles [25]. The case study is representative of summer and demonstrates how the aBLH adjusts to weather conditions around the island. Table 1 outlines the dataset characteristics and indicates consistency in spatial resolution except for NCEP2, which is relegated to synoptic-scale and trend analysis.

**Table 1.** Summary of datasets and horizontal resolution.

| Label | Description | Resolution |
|---|---|---|
| CFS2 | Climate Forecast System Reanalysis version 2 | 30 km |
| Chirp | GOES satellite IR rain estimate from cloud temp and duration | 5 |
| ERA5 | European Community Reanalysis version 5 | 25 |
| GPM | Global Precip. Measurement satellite-gauge version 7 | 10 |
| HYSPLIT | Hybrid Lagrangian Trajectory model airflow | 10 |
| MODIS | Moderate Imaging Sensor IR land surface temperature | 1 |
| NAM | North America Mesoscale model hindcast wind profiles | 10 |
| NCEP2 | National Center for Environ. Pred. Reanalysis version 2 | 180 |

This study aims to understand aBLH modulation in short timescales so that surface–climate coupling and model projections can be more confidently applied to strategic planning decisions over long time scales.

## 3. Results

### 3.1. Observations and Diurnal Cycling

The ERA5 2019–2023 mean aBLH is mapped in Figure 1a together with winds. A zone of shallow aBLH oriented 100–280° overlies the island in contrast with upstream aBLH > 750 m. Diffluent ~090° trade winds of 7 m/s prevail over the sea. The mean annual cycle of aBLH at Mayaguez (Figure 1b) crests in late winter during sunny weather conditions. In contrast, cloudy skies in May and September–November underpin a shallow aBLH. The knock-on effect is that dry spells with high net solar radiation encourage sensible heat flux and surface turbulence that lead to diurnal growth in the aBLH. Table 2 lists the deepest ranked ERA5 hourly aBLH over the period 2019–2023. Numerous February–April cases reach 1900 m when trade winds (U—4 m/s) and net solar radiation (700 W/m$^2$) promote sensible heat fluxes > 300 W/m$^2$ at 13:00. The island's dry turbulence is advected toward Mayagüez, but latent heat fluxes are minimal (100 W/m$^2$) as upstream vegetation is depleted in late winter.

**Table 2.** Deepest aBLH and associated heat fluxes, net solar radiation, and zonal wind.

| Date | Time | aBLH | S.H.F. | L.H.F. | netQs | U Wind |
|---|---|---|---|---|---|---|
| 25 February 2021 | 13:00 | 2027 | 348 | 113 | 841 | −5.1 |
| 13 April 2022 | 13:00 | 1986 | 411 | 128 | 776 | −4.1 |
| 24 February 2021 | 14:00 | 1956 | 292 | 130 | 633 | −3.4 |
| 20 April 2019 | 13:00 | 1922 | 431 | 102 | 804 | −3.1 |
| 20 February 2020 | 13:00 | 1919 | 308 | 134 | 807 | −4.6 |
| 24 March 2023 | 13:00 | 1917 | 379 | 121 | 842 | −2.4 |
| 10 February 2023 | 13:00 | 1912 | 270 | 160 | 730 | −5.9 |
| 19 April 2019 | 12:00 | 1906 | 394 | 100 | 831 | −3.4 |
| 19 February 2019 | 12:00 | 1896 | 261 | 113 | 671 | −4.8 |
| 18 February 2019 | 13:00 | 1879 | 281 | 142 | 816 | −3.7 |
| 12 February 2023 | 14:00 | 1872 | 331 | 156 | 764 | −3.3 |

The mean wind profiles at Mayagüez (Figure 1c) reflect gradients in the surface layer. Sea breezes oppose the trade winds at 1000 hPa (U = 0), but ERA5 zonal winds reach

−6 m/s at 850 hPa. The meridional component reflects Ekman turning as follows: −2 m/s at 1000 hPa, +1 m/s at 925 hPa. Perhaps individual profiles will show a mixed surface layer capped by an inflection but mean profiles exhibit gradual slopes.

East–west sections of mean zonal wind and rainfall on 18.2 N are illustrated in Figure 1d,e. Atmospheric convection increases in proportion to the frictional slowing of trade winds over the island, where dU/dx convergence ($-4 \times 10^{-5}$ s$^{-1}$) sustains uplift after the initial orographic forcing at 65.8 W. The NAM model surface roughness length exceeds 1 m across the island's center from 66.2 to 67 W, where undulating ~ 600 m hills are covered by dense forests. Marine rainfall of 2 mm/day off the east coast doubles over the western half of the island. Frictional slowing of trade winds enables land–sea breezes to concentrate afternoon rainfall. The island footprint is brought out in a latitude–height section of mid-summer mean zonal winds on 67W (Figure 2a). Channelized (U = −10 m/s) airflow in the layer 350–700 m straddles a near-surface wind shadow (−2 m/s) at 18.2 N. Venturi acceleration occurs at 17.5 N and 19.0 N, and the island redirects airflow westward.

The wind rose on the leeward coast of Mayagüez (Figure 2b) indicates that 26% of the time surface winds are <1 m/s (calm), with 31% from the east (45–135°) and 19% from the west (225–315°). Northeast winds are frequent but weak compared with southeast winds. The island wind shadow widens as the Froude number declines [26]. The wind frequency distribution on the windward coast at San Juan (18.5 N, 66.1 W) is quite different (cf. Appendix A, Figure A1a). Only 4% of the surface winds are <1 m/s, 79% of the winds are from the east, and westerlies seldom occur. The synoptic pulsing of the NCEP2 daily dewpoint temperature profile is presented in Figure 2c. From Dec to Mar each year, dry air (Td < 5 °C) subsides in the 2000–3000 m layer. In contrast, moisture builds up (Td > 20 °C) in the 0–500 m layer from July to November. Dry pulsing comes from anticyclonic surges coupled with the Hadley circulation, while moist pulsing derives from transient easterly waves and westerly troughs that bring stormy weather.

The mean Td from the MW profiler reflects two regimes (Figure 2d) characterized by dry conditions from Dec to May and moist conditions from June to November. The seasonal delay corresponds with surface coupling to sea surface temperatures and vegetation transpiration. A noteworthy feature is that the standard deviations of Td tend to increase with height in the cool dry season but decrease with height in the warm moist season. Subsidence above 2000 m during the winter–spring season entrains dry air into the boundary layer, depending on atmospheric stability under the influence of transient synoptic weather systems.

### 3.2. Mean Diurnal Cycle and Correlations

In this section, we analyze the mean diurnal cycle at Mayagüez from 2019 to 2023. CFS2 sensible and latent heat fluxes (Figure 3a,b) show asymmetrical features wherein sensible heat flux rises smoothly after sunrise and then dips around 14:00, and latent heat flux (transpiration) rises gradually after sunrise and then peaks after 14:00. Hence, the surface fluxes reflect rain–evaporation feedback [27,28] with less dry turbulence and greater moist turbulence in the afternoon. Heat flux variance grows from 14:00 to 17:00 because of infrequent convection. The aBLH box–whisker plot (Figure 3c) is somewhat Gaussian and conforms to net solar radiation. The variance in ERA5 aBLH remains steady across the diurnal cycle. Rainfall at Mayagüez is naturally confined to the afternoon hours because land–breeze divergence inhibits convection at night and early in the morning. There is good agreement between the ERA5 + CFS2 model rainfall and GPM satellite rainfall, where both peak at 16:00–17:00. Lag correlations with respect to the Mayagüez hourly aBLH time series in 2023 are presented in Figure 4a. A cascade emerges with peak correlation as follows: r = 0.79 net solar radiation and 0.74 sensible heat flux simultaneously, 0.56 for latent heat flux at +1 h, and 0.16 for rain at a +3 h delay. The r value of −0.42 for U wind at −4 h refers to morning trade winds that amplify and advect diurnal heating to the leeward coast. Auto-correlation resonance is described in Figure 4b, wherein sensible heat flux exhibits large steady day/night oscillations, while U wind remains positive with low amplitude and rain tails off over successive diurnal cycles.

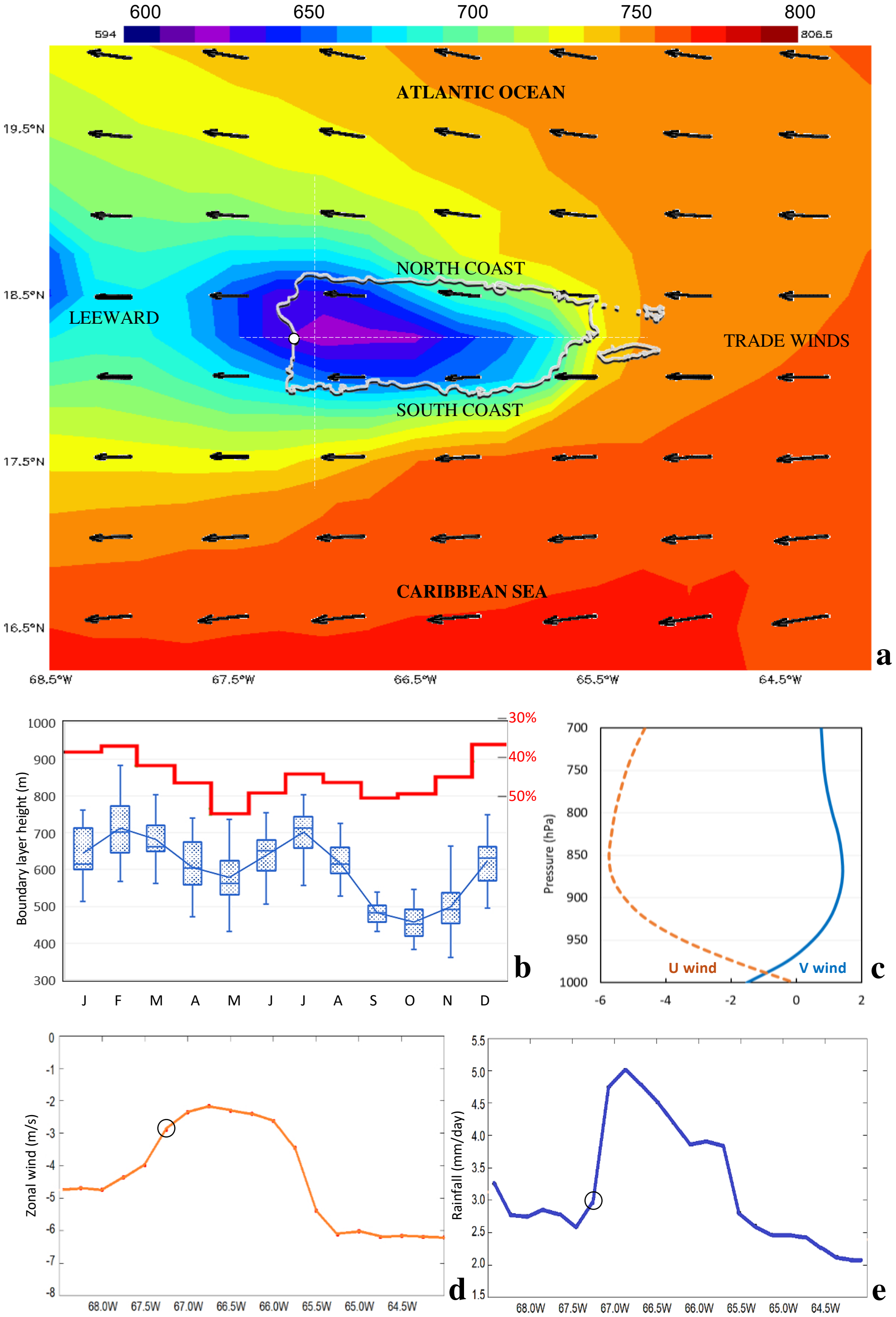

**Figure 1.** (**a**) Map of 2019–2023 mean ERA5 boundary layer height and near-surface wind vectors (max 7 m/s). The dot is Mayagüez, and the dashed lines are sections. (**b**) Mean annual cycle of ERA5 boundary layer height and % cloud cover (inverted red line). (**c**) Mean profiles of ERA5 U, V wind components at Mayaguez (m/s). Mean longitude section on 18.2 N of (**d**) ERA5 zonal wind and (**e**) GPM multi-satellite rainfall. Mayagüez is circled.

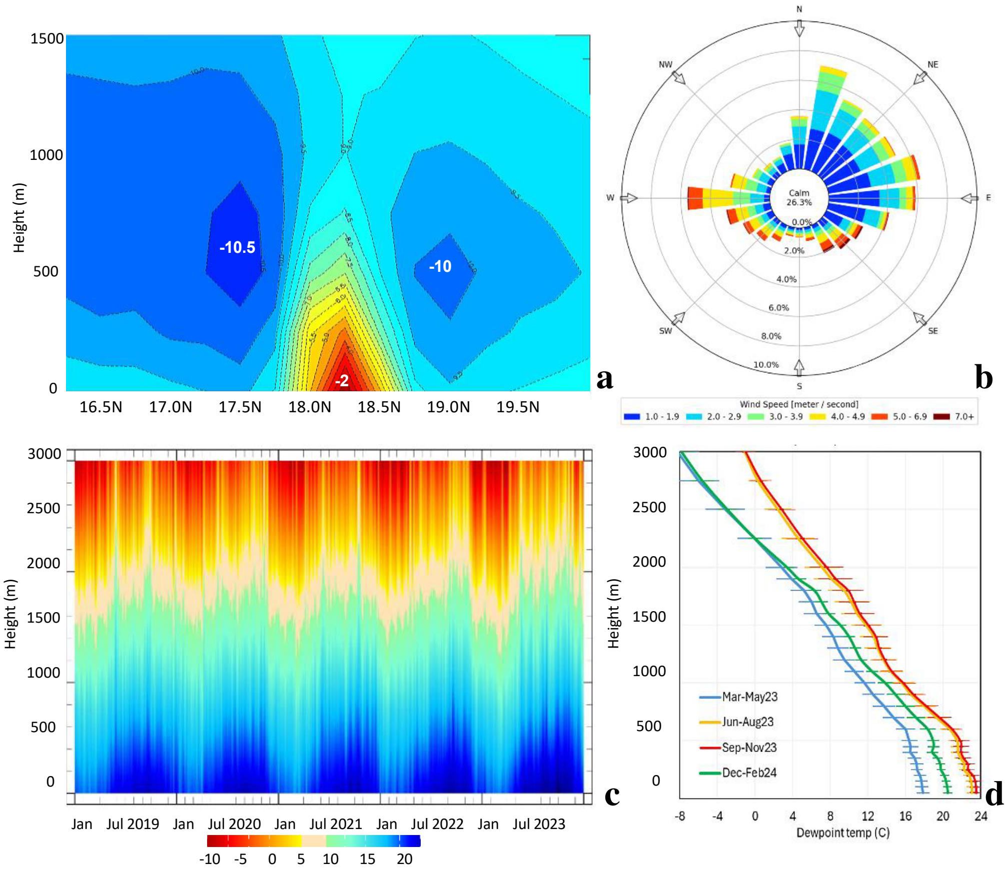

**Figure 2.** (**a**) Latitude–height section of ERA5 June–August mean zonal airflow on 67W. (**b**) Wind rose 2019–2023 at the NOAA station in Mayagüez harbor (18.2° N, 67.15° W). (**c**) Time–height plot of NCEP2 daily dewpoint temperature over Mayagüez. (**d**) Seasonal mean dewpoint temperature from the MW profiler with standard deviation bars.

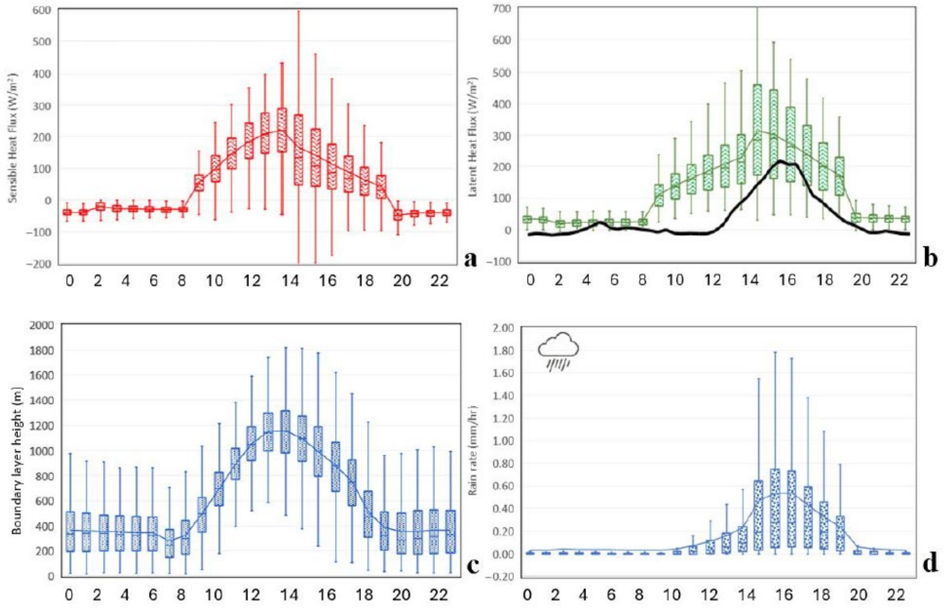

**Figure 3.** Box–whisker plots of the 2019–2023 mean diurnal cycle: (**a**,**b**) CFS2 sensible and latent heat flux, (**c**) ERA5 boundary layer height, and (**d**) ERA5 + CFS2 rainfall at Mayagüez compared with GPM (black line).

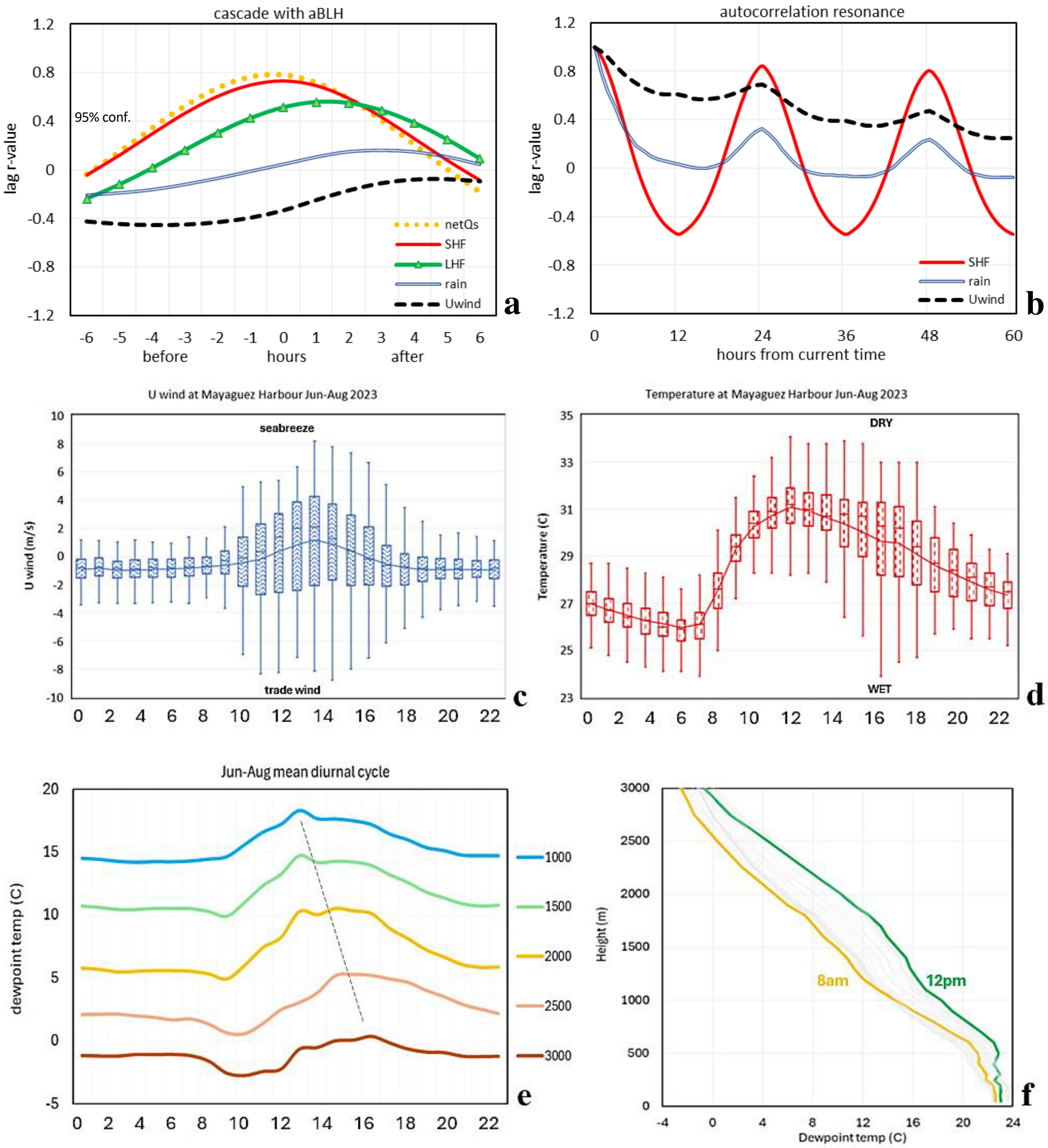

**Figure 4.** (**a**) Lag correlation between the aBLH and hourly data at Mayagüez. (**b**) Auto-correlation 'resonance' of time series N = 8760. Box–whisker plots of June–August 2023 mean diurnal cycle at the NOAA harbor station: (**c**) zonal wind and (**d**) air temperature. Mean diurnal cycle of the dewpoint temperature from the MW profiler in June–August 2023: (**e**) at various levels over time and (**f**) as hourly profiles and (colored) min/max.

A recent summer was examined for diurnal changes in thermodynamic properties. The June–August 2023 period was characterized by anticyclonic trade winds, with ~85% of normal rainfall and fewer storms. The mean diurnal cycle plots of the zonal wind and air temperature measured at Mayagüez harbor (Figure 4c,d) reveal amplitude and phase with some asymmetry. Zonal winds are weak at night at −1 m/s; three hours after sunrise, turbulent mixing builds momentum. The following weather regimes emerge from the hourly statistics: anticyclonic trade winds of −3 m/s from 11:00 to 14:00 and thermal sea breezes of +4 m/s from 13:00 to 16:00. The mean diurnal cycle of air temperature shows little variance in the night and morning hours, followed by rapid warming from 26 °C to 31 °C from 07:00 to 12:00. Around 16:00 h, the air temperature variance grows to a peak of 3 °C because of sporadic rain showers.

The diurnal cycles of Td—analyzed from the MW profiler—are presented in Figure 4e. Td is low and steady during the night and then dips after sunrise as subsidence from land–breeze divergence reaches the upper boundary layer. Moisture spreads upward from a height of 1000 m at 13:00 to 3000 m at 16:00. With a mean aBLH of ~1100 m, one might expect a little diurnal response of Td above that level. However, the MW profiler indicates a 6 °C increase in Td from morning to afternoon at the 2000 m level, as the warm moist layer deepens. Considering the mean Td profiles by hour (Figure 4f), we note a homogeneous layer ~22 °C up to 600 m that accords with moist turbulence from the west coast sea breeze. The mid-day Td profiles show a secondary moist layer of 14 °C at 1400–1700 m associated with transpiration advected from the interior mountains by trade winds. The minimum and maximum Td values occur at 08:00 and 12:00, coinciding with the onset and the peak of the sea breeze, leaving afternoon rain–evaporation feedback as a secondary influence.

### *3.3. Case Study of Diurnal Cloud Bands*

Considering a case study on 8–9 July 2023, we analyzed diurnal weather conditions to illustrate convective coupling and impacts. Maps of satellite daytime land surface temperature and rainfall are presented in Figure 5a,b. Offshore sea surface temperatures were 29 °C, while the coastal plains warmed above 35 °C. Although interior forests remained < 25 °C, thermal forcing drew 8 m/s trade winds onshore, where NOAA stations on the north and south coast registered 13:00 wind directions of 070° and 120°, respectively. Rainfall >30 mm extended in a cloud band ~30 km wide from San Juan to Mayagüez. NAM wind profiles (Figure 5c) indicated steady 9 m/s east–southeast winds above 1500 m. The wind shadow at Mayagüez emerged as a <5 m/s airflow that deepened from 300 m at 06:00 to 1300 m at 15:00.

The station time series (Figure 5d) revealed trade winds during early morning and late afternoon. However, mid-day was characterized by T > 30 °C from 09:00 to 14:00, inducing a westerly sea breeze of ~4 m/s. Temperatures dropped 6 °C during rain showers (38 mm) at 15:00. The aBLH rose from 200 m to 1000 m by noon (Figure 5e). A secondary peak subsequently collapsed by sunset 18:00. Light winds below the aBLH implied that diurnal heating conveyed friction upward, modulating the island wake.

One benefit of diurnal cloud bands is streamflow, which sustains water resources during mid-summer dry spells. In this case, the USGS gauge on the Añasco River increased from 3 to 15 $m^3/s$ by 19:00 (Figure 5e). Elsewhere across the island, river discharge increased 5-fold, although synoptic weather forcing was weak. The diurnal growth in the aBLH corresponded to sea breeze convergence. The dewpoint profiles from in situ measurements at Mayagüez on 9 July 2023 (Figure 5f) confirmed a homogeneous layer 0–600 m of Td ~23 °C and an increase of 1 °C/2 h from morning to afternoon in the 1000–2000 m layer. However, the Td profile exhibited no distinct inflection that might detect an aBLH. We infer the island's moist turbulence is drawn into the cloud band, casting aside the trade wind subsidence.

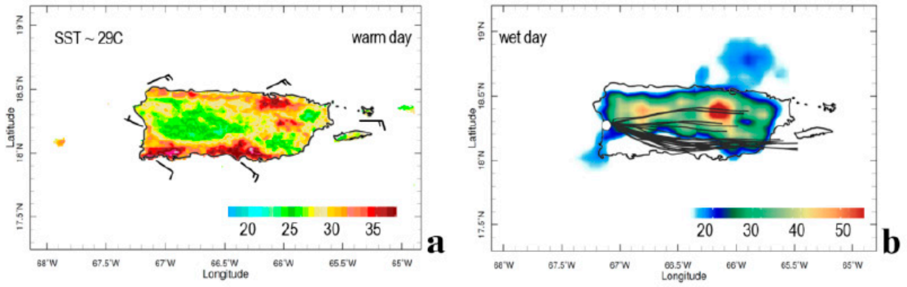

**Figure 5.** *Cont.*

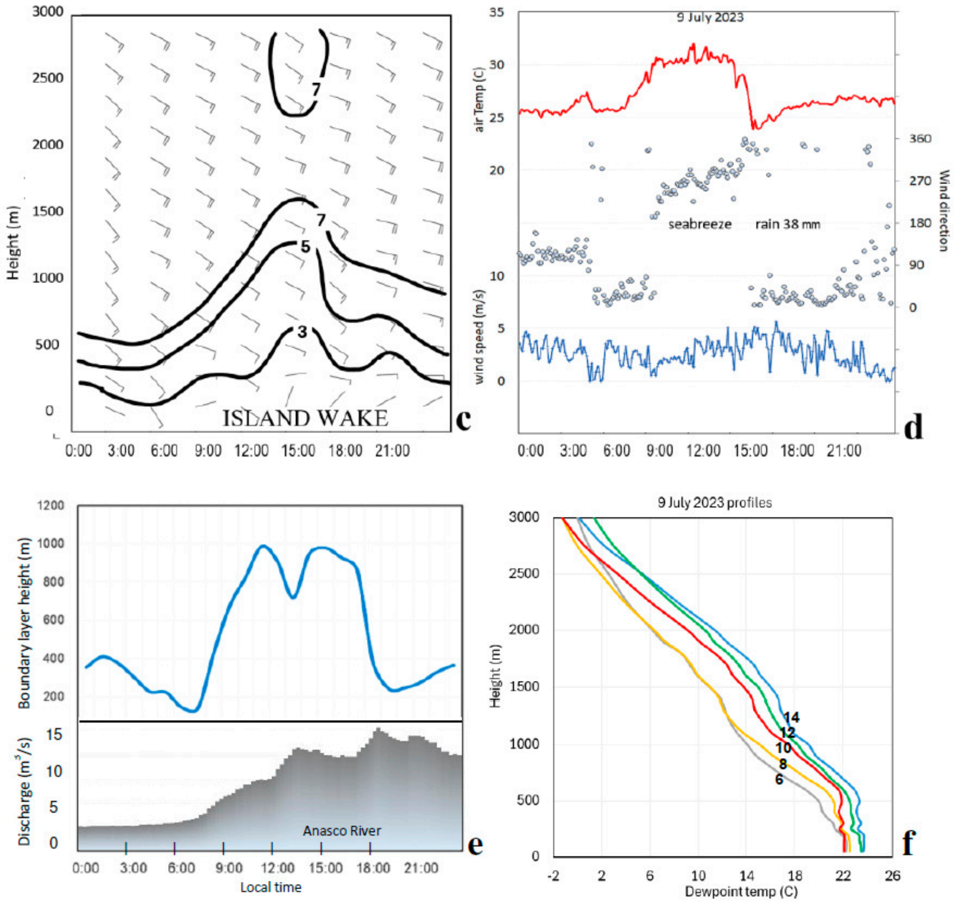

**Figure 5.** Case study of diurnal weather in July 2023. Maps of (**a**) 8 July satellite land surface temperature (C) and NOAA coastal winds at 13:00, (**b**) 9 July daily Chirp rainfall (mm) and daytime back-trajectories. (**c**) Profiles of NAM wind profiles and isotachs (m/s). (**d**) Time series of the NOAA harbor station air temperature, wind direction (dots), and speed (lower). (**e**) Time series of ERA5 hourly boundary layer height and local USGS river discharge (lower). (**f**) MW profiler dewpoint with hours labeled.

### 3.4. EOF Analysis

To place the above work in context, we performed an EOF analysis of GPM monthly rainfall. The outcome has two leading modes illustrated in Figure 6a,b by loading maps as follows: PC-1 'SE marine', accounting for 70% of the total variance, and PC-2 'NW land', with 17% of the total variance. PC-1 extends from the Caribbean Sea, whereas PC-2 is confined to the island and has inverse loading over the ocean. The cumulative time scores (Figure 6c) show how PC-1 forms a base of rainfall that rises with sea surface temperature in late summer, while PC-2 adds to the island rainfall in early summer. In the period 2011–2021, PC-2 cloud bands were of high amplitude. The box–whisker plot of the mean annual cycle for PC-2 (Figure 6d) crests in April–August and shows high variance in mid-summer. Point-to-field correlations were calculated with a number of meteorological variables to understand inter-annual modulation between 2000 and 2023. However, only sensible heat flux gave a significant result (Figure 6e) with an upstream positive signal, indicating that higher sensible heat flux promotes island cloud bands in early summer, similar to [29,30]. There was a negative signal downstream, suggesting convection over Puerto Rico leaves a westward residual effect.

### 3.5. Implication of Climatic Trends

Earlier work has detected climate change signals in surface moistening and drying aloft [31]. A linear trend analysis from 1979 to 2023 was performed to understand how local symptoms relate to global warming. These are presented as profiles of Td and U V

W wind components at Mayagüez in Figure 7a,b. Td shows little trend at the surface but increasing desiccation with height, reaching −0.02 °C/yr at 700 hPa (3000 m), thus confirming previous findings on drying aloft. Vertical motion also shows little trend below 925 hPa but increasing subsidence aloft −0.03 cm $s^{-1}$/yr at 600 hPa. Zonal winds at Mayagüez show a tendency for increased westerlies near the surface and increased easterlies −0.02 m $s^{-1}$/yr above 850 hPa. Meridional (V) winds trend northerly −0.02 m $s^{-1}$/yr from 1000 to 800 hPa (0–2000 m) and weaken aloft.

Regional analysis of trends in the 1000–850 hPa airflow (Figure 7c) reveals that trade winds accelerate and swerve equatorward from 23N to 15N. Cool dry Atlantic air is drawn toward the Caribbean Sea, bringing northerly winds over Puerto Rico. Subsidence is produced by declining Coriolis value, which desiccates the upper boundary layer. Although land surface temperature trends from 2000 to 2023 (Figure 7d) show warming along the south coast (+0.10 °C/yr), interior forests remain cool (−0.05 °C/yr) where summer cloud bands are frequent (cf. Figure 6b, PC2 cluster). We infer that rain–transpiration feedback has increased because of rising CO2 concentrations [32], helping to anchor local convection during mid-summer. Supporting this concept, trends in latent heat flux over western Puerto Rico are upward +0.5 W $m^{-2}$/yr (Appendix A, Figure A1b).

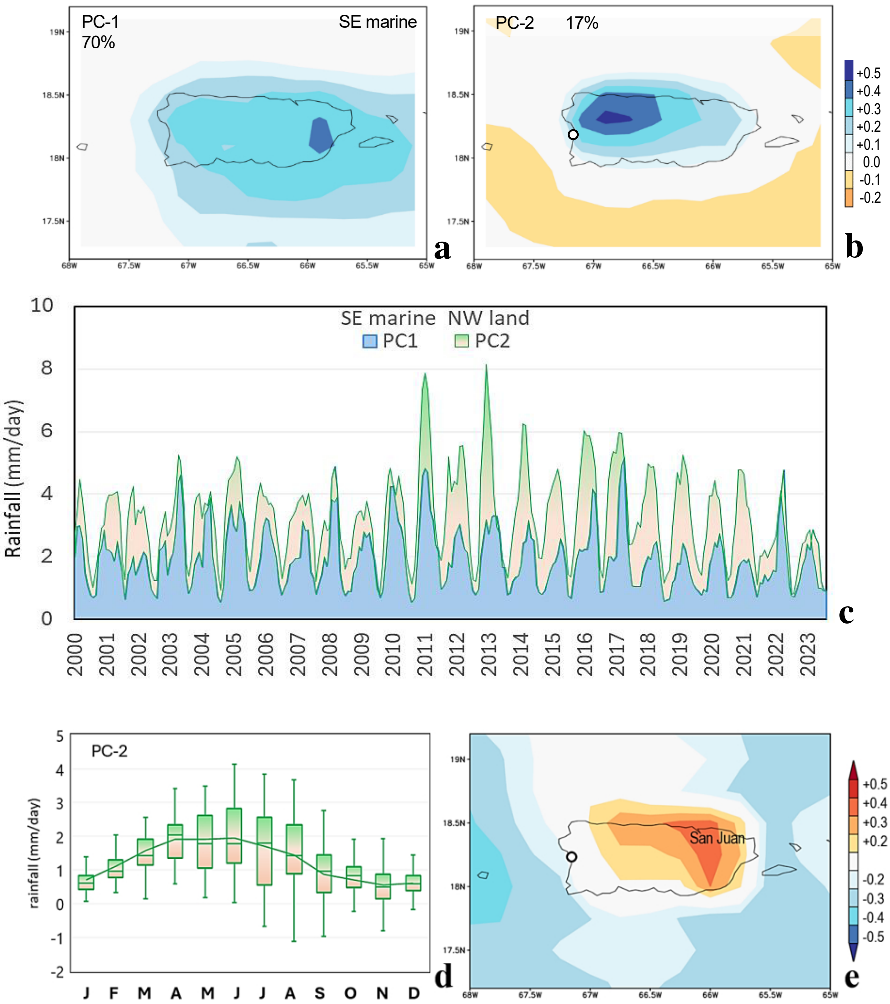

**Figure 6.** EOF analysis of monthly 20 km resolution GPM rainfall from 2000 to 2023: (**a**) PC1 loading, (**b**) PC2 loading, (**c**) respective time scores (stacked), and (**d**) box–whisker plot of the PC2 mean annual cycle. (**e**) Correlation between 25 km resolution ERA5 sensible heat flux and April–August PC2 time score, 95% confidence r > |0.4|.

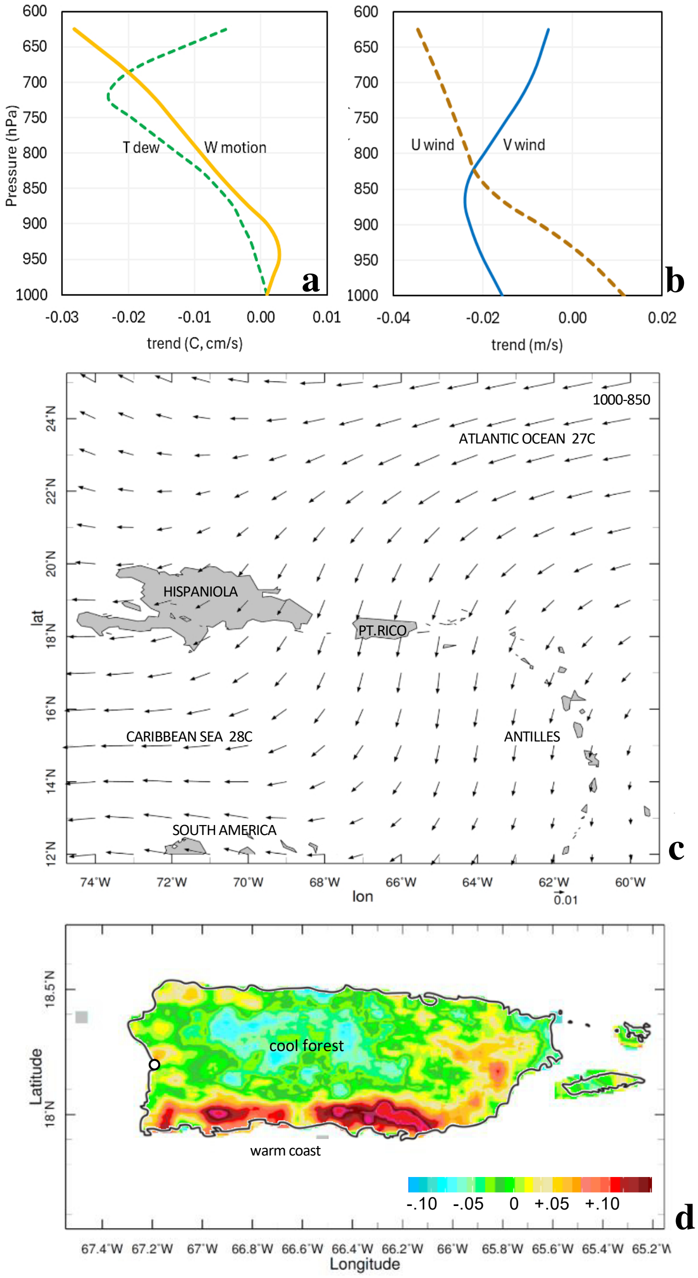

**Figure 7.** Linear trend analysis from 1979 to 2023: (**a**) Mayaguez profiles of ERA5 dewpoint temperature and vertical motion (°C/yr, cm $s^{-1}$/yr) and (**b**) U and V wind (m $s^{-1}$/yr). (**c**) Trend in NCEP2 regional airflow (m $s^{-1}$/yr) and (**d**) trend in MODIS satellite IR daytime land surface temperature 2000–2023 (°C/yr).

## 4. Concluding Discussion

This research explored the average characteristics and hourly to seasonal changes in the atmospheric boundary layer height (aBLH) over a Caribbean island, utilizing a combination of observed and reanalyzed data. Calculations involved long-term averaging, mean diurnal cycle box–whisker plots, frequency distributions, correlation mapping, EOF cluster analysis, and a representative case study—underpinned by hourly in situ and numerically interpolated data. A frictional decrease in easterly winds from 6 to 2 m/s results in a shallow aBLH and a doubling of rainfall over Puerto Rico. Through statistical analyses, this study determined the amplitude and phase of the aBLH and its relationship with meteorological conditions on the leeward coast (18.2 N, 67.1 W). Similar work was reported by [33] during summer over a southern Japanese island.

The following answers to our scientific questions emerged from this study: (i) the aBLH is modulated by net solar radiation, diurnal heat flux, and wind speed, which induce surface turbulence to varying degrees, (ii) the aBLH varies from year to year because of upstream sensible heat flux and airflow trajectory, (iii) the island wind wake, sea breeze convergence, and afternoon convection alter the aBLH on the leeward coast, and (iv) the island's footprint of the aBLH is distinguished in the 25 km reanalysis, but quantitative validation by the in situ MW profiler is outstanding.

The mean annual cycle of the aBLH fluctuates between 500 and 700 m, consistent with local aerosol profiles (Appendix A, Figure A1c) and the findings of [12,17]. Diurnally cycled sensible heat fluxes deepen the aBLH from 300 m at 07:00 to 1200 m by 13:00. Daytime sea breezes >2 m/s converge humidity, as detected by an in situ MW profiler. Rainfall at Mayagüez is concentrated at >0.5 mm/h between 14:00 and 18:00 (cf. Figure 3d), contributing to efficient runoff. The lag correlations with aBLH show a cascade of diurnal heat to moisture conversion, while auto-correlation resonance is strong for sensible heat flux but weak for zonal wind (cf. Figure 4b), suggesting under-representation by the 25 km resolution reanalysis.

This study focused on mid-summer when dry subtropical weather alternates with locally generated convection. The mean diurnal cycle of Td exhibits a 3 °C increase at a 1000 m height at 13:00 h that spreads upward to 3000 m by 16:00 h. Moisture is entrained by deep cumulus clouds, as demonstrated in a case study on 8–9 July 2023. Trade winds of 8 m/s turned 30° onshore during mid-day, causing over 30 mm of rainfall in a 30 × 100 km cloud band, yielding a five-fold increase in river discharge across the island.

Our study was enriched by a 24 yr EOF analysis that distinguished marine and terrestrial modes of rainfall, the latter supported by upstream sensible heat flux yielding cloud bands over the western interior. The EOF analysis links long-term climate to short-term weather. To place this work in the context of climate change, linear trends from 1979 to 2023 were evaluated. The Td profile exhibited a drying trend of −0.02 °C/yr above 1500 m (cf. Figure 7a) because of large-scale subsidence. However, interior forests remained cool and supported an upward trend in latent heat flux of 0.5 $\mathrm{Wm^{-2}}$/yr. These opposing effects have significant implications for water resources and underscore the need to better understand entrainment processes at the top of the atmospheric boundary layer and thermal forced helical circulations.

**Author Contributions:** M.R.J. conceived and wrote up the research, with inputs from J.L.C.-P. and A.Á.-V. provided MW sounder data analysis, H.J.J. oversaw the project and funding. All authors have read and agreed to the published version of the manuscript.

**Funding:** This research was funded by the NOAA Center for Atmospheric Sciences grant number [NA22SEC4810015].

**Institutional Review Board Statement:** Not applicable.

**Informed Consent Statement:** Not applicable.

**Data Availability Statement:** The original contributions presented in the study are included in the article, further inquiries can be directed to the corresponding author.

**Acknowledgments:** We thank the NOAA Center for Atmospheric Sciences (grant #NA22SEC4810015) and JE Serrano Educational Partnership for their support. The UPRM MW profiler is a facility of the Puerto Rico Climate Office. Data and analyses in this study used the following websites: WMO-KNMI Climate Explorer, IRI Climate Library, Univ. Hawaii APDRC, NOAA Ready-ARL, USGS river discharge, NOAA-NDBC coastal stations, and Iowa Environmental Monitoring. Author M.R.J. acknowledges support from the South Africa Dept. of Higher Education.

**Conflicts of Interest:** The authors declare no conflict of interest.

## Appendix A

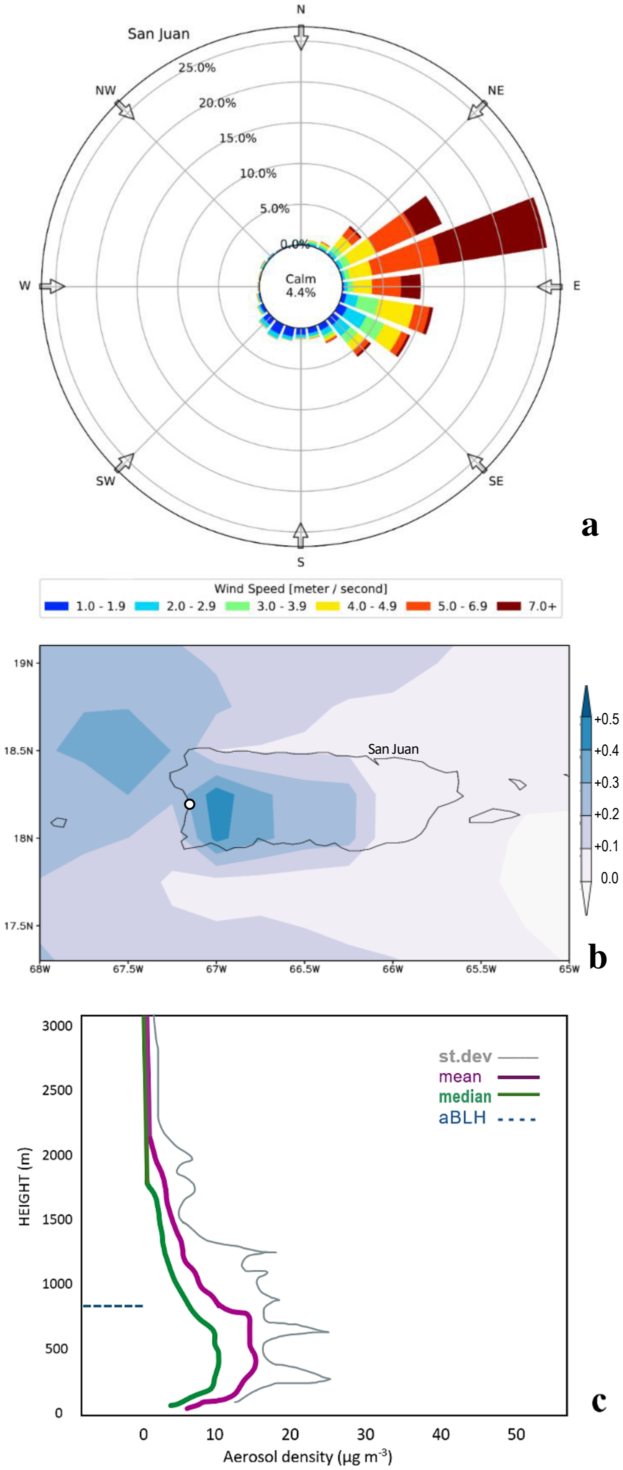

**Figure A1.** (**a**) Wind rose at San Juan harbor for comparison with Figure 2b. Easterlies (45–135°) occur 79% of the time with an average speed of 5 m/s in the period 2019–2023. (**b**) Linear trend in ERA5 latent heat flux (W $m^{-2}$/yr) from 1979 to 2023. (**c**) Calipso long-term mean aerosol profile over Puerto Rico based on 532 nm light extinction.

## References

1. Hendon, H.H.; Woodberry, K. The diurnal cycle of tropical convection. *J. Geophys. Res.* **1993**, *98*, 16523–16637. [CrossRef]
2. Yang, G.Y.; Slingo, J.M. The diurnal cycle in the tropics. *Mon. Weather Rev.* **2001**, *129*, 784–801. [CrossRef]

3. Biasutti, M.; Yuter, S.E.; Burleyson, C.D.; Sobel, A.H. Very high resolution rainfall patterns measured by TRMM precipitation radar: Seasonal and diurnal cycles. *Clim. Dyn.* **2012**, *39*, 239–258. [CrossRef]
4. Jury, M.R.; Chiao, S. Lee-side boundary layer confluence and afternoon thunderstorms over Mayaguez, Puerto Rico. *J. Appl. Meteorol. Climatol.* **2013**, *52*, 439–454. [CrossRef]
5. Kirshbaum, D.J. On thermally forced circulations over heated terrain. *J. Atmos. Sci.* **2013**, *70*, 1690–1709. [CrossRef]
6. Nieves Jiménez, A.T. *Seabreeze, Trade Wind and Terrain Influence on Rainfall Location over Western Puerto Rico*; SOARS UCAR Report; SOARS UCAR: Boulder, CO, USA, 2020; 27p, Available online: https://opensky.ucar.edu/islandora/ (accessed on 1 January 2024).
7. De Wekker, S.F.J.; Kossmann, M. Convective boundary layer heights over mountainous terrain—A review of concepts. *Front. Earth Sci.* **2015**, *3*, 77. [CrossRef]
8. Jury, M.R. Caribbean air chemistry and dispersion conditions. *Atmosphere* **2017**, *8*, 151. [CrossRef]
9. Seidel, D.J.; Ao, C.O.; Li, K. Estimating climatological planetary boundary layer heights from radiosonde observations: Comparison of methods and uncertainty análisis. *J. Geophys. Res. Atmos.* **2010**, *115*, D16113. [CrossRef]
10. Rey-Sanchez, C.; Wharton, S.; de Arellano, J.V.-G.; Paw U, K.T.; Hemes, K.S.; Fuentes, J.D.; Osuna, J.; Szutu, D.; Ribeiro, J.V.; Verfaillie, J.; et al. Evaluation of atmospheric boundary layer height from wind profiling radar and slab models and its responses to seasonality of land cover, subsidence, and advection. *J. Geophys. Res. Atmos.* **2021**, *126*, e2020JD033775. [CrossRef]
11. Jordan, N.S.; Hoff, R.M.; Bacmeister, J.T. Validation of GEOS5-MERRA planetary boundary layer heights using CALIPSO. *J. Geophys. Res. Atmos.* **2010**, *115*, 24218. [CrossRef]
12. Souza, C.M.A.; Dias-Junior, C.Q.; D'Oliveira, F.A.F.; Martins, H.S.; Carneiro, R.G.; Portela, B.T.; Fisch, G. Long-term measurements of the atmospheric boundary layer height in central Amazonia using remote sensing instruments. *Remote Sens.* **2023**, *15*, 3261. [CrossRef]
13. Stull, R.B. *An Introduction to Boundary Layer Meteorology*; Atmospheric & Oceanographic Sciences Library; Springer: Berlin/Heidelberg, Germany, 1988; Volume 13, 684p.
14. Hou, A.Y.; Kakar, R.K.; Neeck, S.; Azarbarzin, A.A.; Kummerow, C.D.; Kojima, M.; Oki, R.; Nakamura, K.; Iguchi, T. The Global Precipitation Measurement mission. *Bull. Am. Meteorol. Soc.* **2014**, *95*, 701–722. [CrossRef]
15. Saha, S.; Moorthi, S.; Wu, X.; Wang, J.; Nadiga, S.; Tripp, P.; Behringer, D.; Hou, Y.-T.; Chuang, H.-Y.; Iredell, M.; et al. The NCEP climate forecast system version 2. *J. Clim.* **2014**, *27*, 2185–2208. [CrossRef]
16. Hersbach, H.; Bell, B.; Berrisford, P.; Hirahara, S.; Horányi, A.; Muñoz-Sabater, J.; Nicolas, J.; Peubey, C.; Radu, R.; Schepers, D.; et al. The ERA5 global reanalysis. *Q. J. R. Meteorol. Soc.* **2020**, *146*, 1999–2049. [CrossRef]
17. Hosannah, N.; Gonzalez, J.E.; Lunger, C.; Niyogi, D. Impacts of local convective processes on rain on the Caribbean Island of Puerto Rico. *J. Geophys. Res. Atmos.* **2019**, *124*, 6009–6026. [CrossRef]
18. Miacci, M.; Angelis, C.F. Ground-based microwave radiometer calibration: An overview. *J. Aerosp. Technol. Manag.* **2018**, *10*, e3518. [CrossRef]
19. Sinclair, V.A.; Ritvanen, J.; Urbancic, G.; Statnaia, I.; Batrak, Y.; Moisseev, D.; Kurppa, M. Boundary-layer height and surface stability at Hyytiala Finland in ERA5 and observations. *Atmos. Meas. Tech.* **2022**, *15*, 3075–3103. [CrossRef]
20. Hannachi, A.; Jolliffe, I.T.; Stephenson, D.B. Empirical orthogonal functions and related techniques in atmospheric science: A review. *Int. J. Climatol.* **2007**, *27*, 1119–1152. [CrossRef]
21. Kanamitsu, M.; Ebisuzaki, W.; Woollen, J.; Yang, S.K.; Hnilo, J.J.; Fiorino, M.; Potter, G.L. NCEP2 reanalysis. *Bull. Am. Meteorol. Soc.* **2002**, *83*, 1631–1643. [CrossRef]
22. Hulley, G.; Freepartner, R.; Malakar, N.; Sarkar, S. *MODIS Land Surface Temperature and Emissivity Product v6*; NASA-GSFC-JPL: Pasadena, CA, USA, 2016.
23. Stein, A.F.; Draxler, R.R.; Rolph, G.D.; Stunder, B.J.B.; Cohen, M.D.; Ngan, F. NOAA HYSPLIT atmospheric transport and dispersion modeling system. *Bull. Am. Meteorol. Soc.* **2015**, *96*, 2059–2077. [CrossRef]
24. Funk, C.C.; Peterson, P.J.; Landsfeld, M.F.; Pedreros, D.H.; Verdin, J.P.; Rowland, J.D.; Romero, B.E.; Husak, G.J.; Michaelsen, J.C.; Verdin, A.P. *A Quasi-Global Precipitation Time Series for Drought Monitoring*; USGS Data Series; US Geological Survey: Reston, VA, USA, 2014. [CrossRef]
25. Janjic, Z. A nonhydrostatic model based on a new approach. *Meteorol. Atmos. Phys.* **2003**, *82*, 271–285. [CrossRef]
26. Jury, M.R.; Chiao, S.; Harmsen, E.W. Mesoscale structure of trade wind convection over Puerto Rico, composite observations and numerical model simulation. *Bound. Layer Meteorol.* **2009**, *132*, 289–313. [CrossRef]
27. Holwerda, F.; Bruijnzeel, L.A.; Scatena, F.N.; Vugts, H.; Meesters, A. Wet canopy evaporation from a Puerto Rican lower montane rain forest: The importance of realistically estimated aerodynamic conductance. *J. Hydrol.* **2012**, *414*, 1–15. [CrossRef]
28. Cronin, T.W.; Emanuel, K.A.; Molnar, P. Island precipitation enhancement and the diurnal cycle in radiative-convective equilibrium. *Q. J. R. Meteorol. Soc.* **2014**, *141*, 1017–1034. [CrossRef]
29. Robinson, F.; Sherwood, S.; Li, Y. Resonant response of deep convection to surface hot spots. *J. Atmos. Sci.* **2008**, *65*, 276–286. [CrossRef]
30. Johnston, M.C.; Holloway, C.E.; Plant, R.S. Sensible heat fluxes control cloud trail strength. *Q. J. R. Meteorol. Soc.* **2023**, *149*, 1165–1179. [CrossRef]
31. Jury, M.R. Inter-comparison of past and projected climate change in Puerto Rico: 1950–2100. *J. Water Clim. Change* **2022**, *13*, 2713–2724. [CrossRef]

32. Alkama, R.; Forzieri, G.; Duveiller, G.G.; Grassi, G.; Liang, S.; Cescatti, A. Vegetation-based climate mitigation in a warmer and greener world. *Nat. Commun.* **2022**, *13*, 606. [CrossRef] [PubMed]
33. Minda, H.; Furuzawa, F.A.; Satoh, S.; Nakamura, K. Convective boundary layer above a subtropical island observed by C-band radar and interpretation using a cloud resolving model. *J. Meteorol. Soc. Jpn.* **2010**, *88*, 285–312. [CrossRef]